AAS 20-594

OBSERVABILITY-AWARE NUMERICAL ALGORITHM FOR ANGLES-ONLY INITIAL RELATIVE ORBIT DETERMINATION

Adam W. Koenig* **and Simone D'Amico†**

This paper presents a simple numerical solution to the problem of estimating the relative orbit of a nearby resident space object using inertial bearing angle measurements from a single monocular camera. Unlike previous approaches, this algorithm provides a covariance for the computed state estimate, is robust to substantial errors in the a-priori state information, and is applicable to any planetary orbit regime as long as accurate models of dominant perturbations are available. This robust performance is enabled by three features of the proposed algorithm. First, leveraging the results of a quantitative observability analysis, the semimajor axis of the observer's orbit is estimated in addition to the relative orbit. Second, the weakly observable range is estimated through a sampling approach and the other strongly observable components are estimated using iterative batch least squares refinement. Third, the uncertainty in the a-priori information is included in the computation of the uncertainty for the estimated state. Monte Carlo simulations using a high-fidelity numerical orbit propagator are conducted to validate the performance of the algorithm and characterize its sensitivity to errors in the a-priori information in both earth and mars orbits. The simulation results show that the proposed algorithm provides relative orbit estimates that are at least as accurate as the best approaches in literature in a wider range of orbit regimes in the presence of larger errors.

INTRODUCTION

The successes of flagship missions such as GRACE (NASA),[1] TanDEM-X (DLR),[2] PRISMA,[3] and the Magnetospheric Multiscale (MMS) mission (NASA)[4] have attracted great interest to formation-flying and spacecraft swarm technologies. A well-known need in these fields is development of low-cost navigation technologies that can be used in the widest possible range of mission scenarios. Vision-based sensors (VBS) hold great promise in this regard due to three advantages: 1) they have minimal mass, power, and volume requirements, 2) they are passive with high-dynamic range, and 3) they are ubiquitous on modern spacecraft in the form of star trackers.

Angles-only navigation is a particularly promising application for vision-based sensors. In this paper, angles-only navigation refers to the general problem of estimating the orbits of objects in close proximity using bearing angle measurements from one or more monocular cameras. The most well-studied variant of this problem consists of estimating the relative orbit of a single resident space object using measurements from a single monocular camera hosted on an observer with a known orbit. This capability was first demonstrated in flight by the ARGON experiment in the PRISMA mission in 2012.[5] A more autonomous demonstration was conducted during the AVANTI experiment in 2016.[6–8] However, both of these experiments relied on a-priori relative state information from NORAD two-line-elements (TLE) to initialize the navigation filter. To enable navigation in more challenging scenarios (e.g. orbiting other planetary bodies), it is necessary to compute initial relative orbit estimates onboard in real-time.

This problem is challenging because angles-only navigation with a single camera is subject to a well-known range ambiguity. Specifically, Woffinden[9] demonstrated that the range is unobservable if the Cartesian relative position evolves according to a homogeneous linear model. This issue was resolved for the ARGON[5] and

*Postdoctoral Scholar, Aeronautics & Astronautics Dept., Durand Building, 496 Lomita Mall, Stanford, CA, 94305.
†Assistant Professor, Aeronautics & Astronautics Dept., Durand Building, 496 Lomita Mall, Stanford, CA, 94305.

AVANTI[8] experiments by regularly executing maneuvers to improve observability. An alternative approach proposed by Geller[10] was to offset the camera from the observer center of mass to enable triangulation of the range. However, this approach does not add sufficient observability to be of practical value at kilometer-level separations. More recent literature has instead focused on use of accurate nonlinear dynamics models to resolve the range. In particular, studies by Lovell[11] and Hu[12] using Lie-derivative criteria have shown that the relative orbit of a target is observable in Keplerian orbits if certain geometric conditions are met. Additionally, recent work by Sullivan[13,14] has demonstrated maneuver-free angles-only relative navigation using an unscented Kalman filter with a nonlinear dynamics model based on relative orbital elements (ROE) in orbit regimes from low earth orbit (LEO) to geostationary orbit (GEO).

However, few approaches to the initial relative orbit determination (IROD) problem using bearing angle measurements properly account for the perturbations affecting the absolute and relative orbits.[15,16] For example, the approach proposed by Garg[17] uses second-order model of the relative dynamics in Cartesian space for unperturbed orbits. Similarly, Geller[18] used an unperturbed linear dynamics model in cylindrical coordinates. A more recent algorithm proposed by Sullivan[13] instead computes a closed-form estimate of the relative state, which is then refined using iterative regularized batch least squares with a measurement model that accounts for the earth oblateness J_2 perturbation. However, the initial estimate is often subject to large errors and does not always converge to the correct range. The best-performing IROD algorithm to date was developed by Ardaens[19] for low earth orbit. By exploiting the separation between strongly and weakly observable components of the ROE, Ardaens computes a one-dimensional set of candidate state estimates with ranges within specified windows using iterative batch least squares. The final state is selected as the candidate estimate with the smallest measurement residuals. This algorithm was tested on flight data from the AVANTI experiment and produced state estimates with range errors of less than 10% in a small number of test cases. However, these algorithms are still subject to three major limitations: 1) range of applicability (separation between the observer and target, orbit eccentricity, and perturbation environment), 2) reliance on accurate a-priori knowledge of the observer's absolute orbit, and 3) inability to provide an uncertainty estimate that is consistent with estimation errors in realistic test cases.

This paper aims to overcome these limitations by providing a new observability-aware IROD algorithm that 1) provides estimates of the relative orbit of a resident space object and a subset of the observer's absolute orbit elements and corresponding uncertainties, 2) is valid in the widest possible range of planetary orbit regimes, and 3) is maximally tolerant to errors in the a-priori information (the observer's orbit and ballistic parameters). When included with image processing and measurement assignment algorithms such as those proposed by Kruger,[20] such an algorithm could enable fully autonomous angles-only navigation for novel mission architectures, some of which will be tested as part of the Starling Formation-Flying Optical eXperiment (StarFOX) on the NASA Starling1 mission in 2021.[14,21] Within this context, the contributions of this paper to the state of the art are twofold. First, a quantitative observability analysis is conducted to characterize the feasibility of estimating absolute orbit elements of the observer and ballistic parameters in addition to the relative orbit of the target using bearing angle measurements from a single camera in various orbit regimes. Second, a new IROD algorithm inspired by the works of Sullivan[13] and Ardaens[19] is proposed. Leveraging the findings of the observability analysis, the proposed algorithm also estimates the semimajor axis of the observer's orbit in addition to the relative orbit of the target. Additionally, the employed numerical dynamics model incorporates any user-specified perturbations (enabling use in arbitrary planetary orbit regimes) and exploits Gauss's variational equations to provide accurate modeling at low computation cost. The algorithm is validated through Monte Carlo simulations using a high-fidelity numerical orbit propagator[22] and representative error sources in LEO, GEO, and mars orbit, which differ in eccentricity and dominant perturbations. These simulations show that the algorithm can exceed the estimation accuracy of current state-of-the-art algorithms in diverse and challenging scenarios. Overall, these results show that the proposed algorithm can enable autonomous angles-only navigation in the StarFOX experiment and other novel mission applications.

MODELING PRELIMINARIES

Proper selection of the estimated state and measurements is of critical importance to maximize estimation accuracy using angles-only navigation techniques due to the well known weak observability. The estimated

state and its relationship to the measurement model are described in the following.

State and Measurement Definitions

The complete state of the system studied in this paper includes the absolute orbit of the observer, the relative orbit of the target, and the ballistic properties of the spacecraft (if non-conservative perturbations are significant). The absolute and relative orbits are parameterized using the osculating (i.e. instantaneous) quasi-nonsingular absolute orbit elements of the observer, denoted $\boldsymbol{\alpha}$ and the osculating quasi-nonsingular ROE of the target with respect to the observer as defined by D'Amico,[23] denoted $\delta\boldsymbol{\alpha}$. These absolute and relative states are defined as

$$\boldsymbol{\alpha} = \begin{pmatrix} a \\ e_x \\ e_y \\ i \\ \Omega \\ u \end{pmatrix} = \begin{pmatrix} a \\ e\cos(\omega) \\ e\sin(\omega) \\ i \\ \Omega \\ \omega + M \end{pmatrix} \qquad \delta\boldsymbol{\alpha} = \begin{pmatrix} \delta a \\ \delta\lambda \\ \delta e_x \\ \delta e_y \\ \delta i_x \\ \delta i_y \end{pmatrix} = \begin{pmatrix} (a_t - a_o)/a_o \\ u_t - u_o + \cos(i_o)(\Omega_t - \Omega_o) \\ e_{x,t} - e_{x,o} \\ e_{y,t} - e_{y,o} \\ i_t - i_o \\ \sin(i_o)(\Omega_t - \Omega_o) \end{pmatrix} \tag{1}$$

where a the semimajor axis, e is the eccentricity, i is the inclination, Ω is the right ascension of the ascending node (RAAN), ω is the argument of perigee, and M is the mean anomaly. Correspondingly, e_x and e_y are the components of the eccentricity vector and u is the mean argument of latitude. In the relative state definition, elements of the observer and target orbits are indicated by subscript o and t, respectively.

These state definitions were selected for three reasons. First, as noted by Gaias,[24] the relative state definition decouples the weakly observable range (which resides primarily in $\delta\lambda$ in most formation flying scenarios) from other strongly observable state components. Accordingly, weakly and strongly observable states can be estimated with different techniques at minimal computation cost. Second, the absolute orbit state definition allows independent determination of parameters such as orbit period, eccentricity, and orientation through estimation of a subset of the orbit elements. Finally, these slowly varying states facilitate accurate modeling of the absolute and relative motion of the observer and target at low computation cost by numerically integrating Gauss' variational equations with large time steps[13] or using analytical models for specific orbit regimes.[15,16] With these advantages, the algorithm proposed in this paper can be applied to any orbit regime as long as the dominant perturbations are included in the dynamics model.

When non-conservative perturbations (atmospheric drag and solar radiation pressure (SRP)) are non-negligible, the state also includes the ballistic coefficient of the observer, denoted B_o, and the differential ballistic coefficient of the target with respect to the observer, denoted δB. These quantities are defined as

$$B_o = \frac{C_o A_o}{m_o} \qquad \delta B = B_t - B_o \tag{2}$$

where C is the reflectance or drag coefficient, A is the cross-sectional area, and m is the mass of the spacecraft. This definition is preferred over its inverse because the relative acceleration caused by the perturbation increases linearly with the ballistic coefficient, resulting in a more linear behavior of the measurement model with respect to the state. The absolute and differential ballistic coefficients are hereafter assumed to be time-invariant for simplicity.

The bearing angle measurements used to estimate the absolute and relative states are defined as follows. Let $\boldsymbol{r}_o^{\mathcal{I}}$ and $\boldsymbol{r}_t^{\mathcal{I}}$ denote the positions of the observer and target defined in the earth-centered inertial (ECI) frame at some specified epoch. The relative position in the sensor frame, denoted $\delta\boldsymbol{r}^{\mathcal{V}}$, is related to these quantities by

$$\delta\boldsymbol{r}^{\mathcal{V}} = \boldsymbol{R}^{\mathcal{I}\to\mathcal{V}}(\boldsymbol{r}_t^{\mathcal{I}} - \boldsymbol{r}_o^{\mathcal{I}}) \tag{3}$$

where $\boldsymbol{R}^{\mathcal{I}\to\mathcal{V}}$ is the matrix defining the rotation from the inertial to the sensor frame (which is readily provided by any star tracker camera). The bearing angle vector $\boldsymbol{z}$ considered in this paper includes the azimuth ψ and elevation ϕ angles, which are functions of the components of $\delta\boldsymbol{r}^{\mathcal{V}}$ as given by

$$\boldsymbol{z} = \begin{pmatrix} \psi \\ \phi \end{pmatrix} = \begin{pmatrix} \arcsin\left(\delta r_y^{\mathcal{V}}/||\delta\boldsymbol{r}^{\mathcal{V}}||\right) \\ \arctan\left(\delta r_x^{\mathcal{V}}/\delta r_z^{\mathcal{V}}\right) \end{pmatrix}. \tag{4}$$

These angles are nonsingular within the field of view of a star tracker.

Numerical Measurement and Sensitivity Model

The algorithm proposed in this paper requires a model that provides the bearing angles at time t as a function of the system state $\boldsymbol{x}$ (including $\boldsymbol{\alpha}$, $\delta\boldsymbol{\alpha}$, B_o, and δB) at the estimation epoch t_{est} of the form

$$\boldsymbol{z}(t) = \boldsymbol{h}(\boldsymbol{x}, t_{est}, t) \tag{5}$$

Also, as the algorithm does not estimate the complete state of the system, it is instructive to divide $\boldsymbol{x}$ into two partitions including 1) components that are estimated (denoted $\boldsymbol{x}_{est}$) and 2) components that are provided a-priori (denoted $\boldsymbol{x}_{prior}$) as given by

$$\boldsymbol{x} = \begin{pmatrix} \boldsymbol{x}_{est} \\ \boldsymbol{x}_{prior} \end{pmatrix} \tag{6}$$

Next, suppose bearing angles are provided at N epochs $t_1, \ldots, t_N$, which are collectively denoted $\boldsymbol{t}_m$. The batch measurement vector $\boldsymbol{y}$ is obtained by stacking the bearing angle vectors for each epoch. Accordingly, the modeled batch of measurements $\boldsymbol{y}$ can be expressed as

$$\boldsymbol{y} = \boldsymbol{g}(\boldsymbol{x}, t_{est}, \boldsymbol{t}_m) = \begin{pmatrix} \boldsymbol{h}(\boldsymbol{x}, t_{est}, t_1) \\ \vdots \\ \boldsymbol{h}(\boldsymbol{x}, t_{est}, t_N) \end{pmatrix} \tag{7}$$

This measurement model requires propagation of the orbits of the observer and target from t_{est} to each measurement epoch. This is accomplished by Euler integration of Gauss' variational equations including all major perturbations for the considered orbit, allowing large time steps without loss of accuracy.[13] For the state definition adopted in this paper, the osculating orbit elements for each spacecraft evolve according to

$$\dot{\boldsymbol{\alpha}} = \begin{pmatrix} 0 \\ 0 \\ 0 \\ 0 \\ 0 \\ \sqrt{\frac{\mu}{a^3}} \end{pmatrix} + \begin{bmatrix} \frac{2a^2 e \sin(\nu)}{h} & \frac{2a^2 p}{rh} & 0 \\ \frac{p\sin(\theta)}{h} & \frac{((p+r)\cos(\theta)+re_x)}{h} & \frac{re_y \sin(\theta)\cot(i)}{h} \\ -\frac{p\cos(\theta)}{h} & \frac{((p+r)\sin(\theta)+re_y)}{h} & -\frac{re_x \sin(\theta)\cot(i)}{h} \\ 0 & 0 & \frac{r\cos(\theta)}{h} \\ 0 & 0 & \frac{r\sin(\theta)}{h\sin(i)} \\ -\frac{pe\cos(\nu)}{h(1+\eta)} - \frac{2\eta r}{h} & \frac{(p+r)e\sin(\nu)}{h(1+\eta)} & -\frac{r\sin(\theta)\cot(i)}{h} \end{bmatrix} \boldsymbol{d} \tag{8}$$

where h is the angular momentum, ν is the true anomaly, p is the semilatus rectum, r is the orbit radius, $\theta = \nu + \omega$ is the true argument of latitude, and $\boldsymbol{d}$ is the perturbing acceleration defined in the local radial/tangential/normal (RTN) frame to the time derivatives of the orbit elements. The RTN frame is formally defined as follows. The radial direction is aligned with the absolute position vector, the normal direction is aligned with the angular momentum vector, and the tangential direction completes the right-handed triad. The perturbing accelerations for each considered orbit and integration time steps are provided in the corresponding sections of the paper.

The observability analysis and estimation algorithm presented in this work also require evaluation of the partial derivatives of the measurements with respect to each component of $\boldsymbol{x}_{est}$ and $\boldsymbol{x}_{prior}$. To simplify notation in later derivations, the matrices $\mathbf{Y}_{est}$ and $\mathbf{Y}_{prior}$ are defined as

$$\mathbf{Y}_{est}(\boldsymbol{x}) = \left.\frac{\partial \boldsymbol{g}(\boldsymbol{x}, t_{est}, \boldsymbol{t}_m)}{\partial \boldsymbol{x}_{est}}\right|_{\boldsymbol{x}} \qquad \mathbf{Y}_{prior}(\boldsymbol{x}) = \left.\frac{\partial \boldsymbol{g}(\boldsymbol{x}, t_{est}, \boldsymbol{t}_m)}{\partial \boldsymbol{x}_{prior}}\right|_{\boldsymbol{x}} \tag{9}$$

These partial derivatives are computed numerically via a central difference scheme of the form

$$\left.\frac{\partial \boldsymbol{h}}{\partial x}\right|_{\boldsymbol{x}} = \frac{\boldsymbol{h}(\boldsymbol{x} + \Delta\boldsymbol{x}, t_{est}, t) - \boldsymbol{h}(\boldsymbol{x} - \Delta\boldsymbol{x}, t_{est}, t)}{2||\Delta\boldsymbol{x}||} \tag{10}$$

where $\Delta\boldsymbol{x}$ a vector that is zero for all state components except for which the sensitivity is being evaluated. The increment sizes used for the central difference are 10m for the semimajor axis, 10m/a_o for all other absolute orbit elements, 1m/a_o for all ROE, and 0.0001m^2/kg for the absolute and differential ballistic coefficients.

OBSERVABILITY ANALYSIS

While the observability of the relative orbit using angles-only measurements has been widely studied in literature, the problem of simultaneously estimating the absolute orbit of the observer and the relative orbit of the target has received little attention. The most notable study of this problem was conducted by Hu,[12] which concluded that the orbits of two spacecraft in Keplerian orbits are not fully observable with angles-only measurements. However, this study neglects the effects of perturbations that may improve observability. Additionally, even if the complete state is not observable, there is still value in estimating a subset of the state elements. By including components of the absolute orbit in the estimated state, it is possible to relax the accuracy requirements posed on a-priori information, thereby widening the range of mission architectures suitable for angles-only navigation.

With this in mind, the quantitative observability analysis presented in the following will be used to determine which absolute orbit elements and ballistic parameters can be estimated with useful accuracy. This analysis is based on the model for the relationship between the covariance matrix for the complete measurement batch (denoted $\mathbf{R}$) and the covariance matrix for the estimated state (denoted $\mathbf{P}_{est}$) given by

$$\mathbf{R} = \mathbf{Y}_{est}(\boldsymbol{x})\mathbf{P}_{est}\mathbf{Y}_{est}^{T}(\boldsymbol{x}) \tag{11}$$

If $\mathbf{Y}_{est}$ is full column rank (which is the case for every scenario assessed in this paper), $\mathbf{P}_{est}$ can be expressed as

$$\mathbf{P}_{est} = (\mathbf{Y}_{est}^{T}(\boldsymbol{x})(\mathbf{Y}_{est}(\boldsymbol{x}))^{-1}(\mathbf{Y}_{est}^{T}(\boldsymbol{x})\mathbf{R}\mathbf{Y}_{est}(\boldsymbol{x}))(\mathbf{Y}_{est}^{T}(\boldsymbol{x})\mathbf{Y}_{est}(\boldsymbol{x}))^{-1} \tag{12}$$

This approach is preferred over other techniques such as Lie derivatives or evaluating the condition number of the observability Gramian because the terms of $\mathbf{P}_{est}$ can be declared directly with accuracy requirements for applications of interest.

Next, it is necessary develop a model for $\mathbf{R}$. In this paper, it is assumed that two factors contribute to $\mathbf{R}$: 1) sensor noise (denote $\mathbf{R}_{sensor}$), and 2) uncertainty in a-priori state information (denoted $\mathbf{P}_{prior}$. Under this assumptions, $\mathbf{R}$ can be formulated as

$$\mathbf{R} = \mathbf{R}_{sensor} + \mathbf{Y}_{prior}(\boldsymbol{x})\mathbf{P}_{prior}\mathbf{Y}_{prior}^{T}(\boldsymbol{x}) \tag{13}$$

It should be noted that $\mathbf{R}_{sensor}$ denotes the covariance for the complete batch of N measurements. Under the assumption that all measurements are independent with identical noise distributions, this matrix is related to the measurement noise matrix for a single measurement $\mathbf{R}_1$, by

$$\mathbf{R}_{sensor} = \begin{bmatrix} \mathbf{R}_1 & \mathbf{0} & \dots & \mathbf{0} \\ \mathbf{0} & \mathbf{R}_1 & \dots & \mathbf{0} \\ \vdots & \vdots & \ddots & \vdots \\ \mathbf{0} & \mathbf{0} & \dots & \mathbf{R}_1 \end{bmatrix} \tag{14}$$

For simplicity, it is assumed in this section that $\mathbf{P}_{prior} = \mathbf{0}$. Also, it should be noted that this model assumes perfect knowledge of the system dynamics. Under these optimistic assumptions, the computed values of $\mathbf{P}_{est}$ are effectively lower bounds on the achievable estimation uncertainty.

The authors computed covariance matrices for various sets of estimated state components for scenarios in three different orbit regimes. The first orbit is a sun-synchronous LEO, which is representative of the StarFOX experiment[14,21] and most formation flying missions to date. The second orbit is and eccentric mars orbit similar to the Mars Express mission.[25] The third orbit is a GEO, which is used to assess the impact of the non-conservative SRP perturbation. For each absolute orbit, covariance matrices are computed for two relative orbits. The first relative orbit provides long-term passive safety via relative eccentricity/inclination vector separation[26] and is typical of formation flying missions. The second relative orbit provides a near

Table 1. Initial osculating absolute and relative orbits for observability analysis

	Observer absolute orbits					
	a (km)	e_x (-)	e_y (-)	i (deg)	Ω (deg)	u (deg)
LEO	6978	0.0014	0.0014	98.0	60.0	30.0
Mars	8600	0.0000	-0.5710	93.0	0.0	-45.0
GEO	42164	0.0007	0.0007	6.0	45.0	45.0
	Relative orbits of target					
	$a_o\delta a$ (m)	$a_o\delta\lambda$ (km)	$a_o\delta e_x$ (m)	$a_o\delta e_y$ (m)	$a_o\delta i_x$ (m)	$a_o\delta i_y$ (m)
ROE1	0.0	50.0	0.0	2000.0	0.0	2000.0
ROE2	0.0	50.0	0.0	0.0	0.0	0.0

constant along-track separation, which is known to be less observable in scome scenarios.[11,12] The absolute and relative orbits for these test cases are provided in Table 1. The ROE are multiplied by a_o to provide a geometric interpretation of the relative motion.

It is assumed that the bearing angles at each measurement epoch are subject to noise with covariance given by $\mathbf{R}_1 = 9.4 \times 10^{-9}\mathbf{I}^{2\times2}$, which is equivalent to 20arcsec (1-σ) uncertainty. This is representative of expected errors from current state-of-the-art star tracker cameras.[27] It is also assumed that 50 measurements are provided per orbit in evenly spaced intervals to enable proper comparison across orbit regimes. These correspond to sample times of 120s in LEO, 480s in Mars orbit, and 1800s in GEO, which are easily achievable by any star tracker camera. This measurement frequency is more than sufficient to provide accurate sampling of the short-period effects of low order gravitational harmonics, solar radiation pressure, and third body gravity.

LEO Results

The LEO orbit has a high enough altitude ($\sim$600km) that the effects of atmospheric drag can be neglected. Accordingly, the dynamics model is implemented with a 2x2 gravity field using GRACE gravity model 01S[1] and a time step of 30 seconds. Covariance matrices are computed for two orbits of measurements for each of four sets of state components. Each state set includes the complete relative orbit of the target and the following subsets of the observers absolute orbit elements: 1) nothing, 2) a, 3) e_x, e_y, i, and Ω, and 4) u. The 1-σ uncertainty for each estimated state element in these tests are provided in Table 2. Each uncertainty is computed by taking the square root of corresponding element on the main diagonal of the covariance matrix. Also, the uncertainties of all elements except the semimajor axis are scaled by the semimajor axis to provide a geometric interpretation of the navigation accuracy. Several conclusions can be drawn from the results

Table 2. Uncertainties for each subset of estimated states with two orbits of measurements in LEO.

ROE	1	1	1	1	2	2	2	2
$a\sigma_{\delta a}$ (m)	2.2	2.3	2.5	2.3	12.1	44.1	136.8	12.1
$a\sigma_{\delta\lambda}$ (km)	0.7	0.7	1.3	37.3	3.6	12.2	39.0	163.4
$a\sigma_{\delta e_x}$ (m)	0.7	0.7	7.0	5.4	0.9	1.3	191.7	0.9
$a\sigma_{\delta e_y}$ (m)	25.3	25.6	54.3	1491.5	0.7	1.0	213.4	1.3
$a\sigma_{\delta i_x}$ (m)	0.7	0.7	26.7	5.3	0.7	0.7	164.7	0.7
$a\sigma_{\delta i_y}$ (m)	25.2	25.5	54.5	1491.4	0.7	0.7	190.6	0.7
σ_a (m)	-	13.9	14.9	-	-	48.7	344.9	-
$a\sigma_{e_x}$ (km)	-	-	0.7	-	-	-	29.8	-
$a\sigma_{e_y}$ (km)	-	-	1.0	-	-	-	26.3	-
$a\sigma_i$ (km)	-	-	1.6	-	-	-	26.8	-
$a\sigma_{\delta\Omega}$ (km)	-	-	3.9	-	-	-	23.2	-
$a\sigma_{\delta u}$ (km)	-	-	-	18.6	-	-	-	81.7

for ROE1. First, inclusion of the semimajor axis in the estimated state has negligible impact on estimation

accuracy for the relative orbit. Accordingly, it is advisable to estimate the semimajor axis unless the a-priori information is very accurate (¡15m error). Second, the uncertainties $\delta\lambda$, δe_y, and δi_y are all $<2\%$ of their nominal values (see ROE1 definition in Table 1), indicating that the majority of the uncertainty lies in the range to the target. Third, it is clear that the absolute eccentricity vector, inclination, and RAAN cannot be estimated with an accuracy of better than 1km. Accordingly, these elements should not be estimated unless a-priori information is subject to very large errors. Finally, including u in the estimated state causes a large increase in the range uncertainty. In addition to demonstrating that estimating u is infeasible, this result suggests a strong correlation between the error in the estimated range and the error in the a-priori value of u. The trends for ROE2 are similar to those for ROE1, but the uncertainty in range is approximately five times larger. It is clear from these trends that purely in-train formations are characterized by poor observability (particularly due to difficulty distinguishing between $\delta\lambda$ and δa). As such, additional mitigations such as maneuvers or use of multiple observers will be needed in these scenarios.

The large increase in the range uncertainty that is observed when u is estimated has a geometric interpretation that can be understood by considering the eigenvector corresponding to the largest eigenvalue of the covariance matrix. These eigenvectors for an estimated state including the ROE and u for each considered ROE are provided in Table 3. These eigenvectors have two common properties. First, the vector formed by

Table 3. Maximum singular vectors when estimating u.

State component	δa	$\delta\lambda$	δe_x	δe_y	δi_x	δi_y	u
ROE1	0.0000	0.8919	0.0001	0.0356	-0.0001	0.0355	-0.4494
ROE2	0.0002	0.9037	0.0000	0.0000	0.0000	-0.0002	-0.4737

the ROE components is almost exactly parallel to the ROE state vectors as specified in Table 1, indicating uncertainty in range. Second, the component corresponding to u is very close to negative one half of the $\delta\lambda$ component. Together, these behaviors suggest that there is a poorly observable mode where any error in u will cause an error in $\delta\lambda$ that is opposite in sign and twice as large. This behavior is expected given the geometry of relative motion in near circular orbits as notionally illustrated in Figure 1.

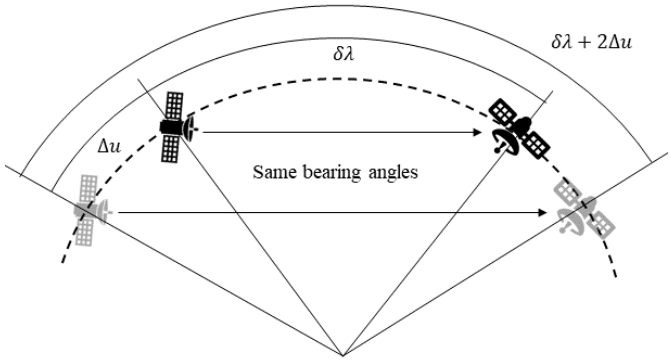

Figure 1. Conceptual illustration of the poorly observable mode when mean argument of latitude is estimated in near-circular orbits.

Mars Orbit Results

Since higher order gravitational perturbations are more significant in Mars orbit than Earth orbit, the dynamics model used for the Mars orbit test cases includes a 4x4 GMM3 gravity field[28] and uses a 60 second time step. Covariance matrices for same estimated state component sets considered in LEO were computed

for the Mars orbit in Table 1 with two orbits of measurements. The uncertainties for each estimated state component in these tests are provided in Table 4. The trends in this table generally follow those in Table 2 with two noteworthy differences. First, inclusion of the semimajor axis in the estimated state increases range uncertainty by roughly a factor of two, but the uncertainty is still smaller than observed in LEO. Second, the uncertainty in the range for ROE2 is similar to the range uncertainty for ROE1. These behaviors clearly show that orbit eccentricity and larger perturbations introduce nonlinearities in the bearing angle measurements that improve observability of the absolute and relative orbits.

Table 4. Uncertainties for each subset of estimated states in Mars orbit.

ROE	1	1	1	1	2	2	2	2
$a\sigma_{\delta a}$ (m)	0.6	0.6	1.7	0.6	0.6	0.6	4.9	0.6
$a\sigma_{\delta\lambda}$ (km)	0.2	0.5	0.9	5.8	0.3	0.5	2.4	75.1
$a\sigma_{\delta e_x}$ (m)	0.4	0.4	0.5	0.5	0.4	0.4	0.5	0.5
$a\sigma_{\delta e_y}$ (m)	9.2	18.2	33.0	233.2	0.9	0.9	4.3	0.9
$a\sigma_{\delta i_x}$ (m)	0.3	0.3	0.6	0.3	0.3	0.3	0.5	0.3
$a\sigma_{\delta i_y}$ (m)	9.7	18.5	34.5	233.3	0.7	0.7	2.8	0.7
σ_a (m)	-	14.6	14.8	-	-	14.6	15.6	-
$a\sigma_{e_x}$ (km)	-	-	0.3	-	-	-	0.9	-
$a\sigma_{e_y}$ (km)	-	-	0.1	-	-	-	0.1	-
$a\sigma_i$ (km)	-	-	0.5	-	-	-	0.5	-
$a\sigma_{\delta\Omega}$ (km)	-	-	0.3	-	-	-	0.3	-
$a\sigma_{\delta u}$ (km)	-	-	-	2.9	-	-	-	37.5

GEO Results

Observability in GEO is assessed using a dynamics model that includes a 2x2 gravity field, solar radiation pressure, and third body gravity from the sun and moon and a 900 second timestep. Noting the poor observability for absolute orbit elements other than the semimajor axis in LEO and Mars orbits, the estimated state subsets considered for this analysis include the ROE augmented with 1) nothing, 2) a, 3) B_o, and, 4) δB. Covariance matrices were computed for two orbits of measurements under the assumption that $B_o = \delta B =$ 0.01 m^2/kg, which is consistent with CubeSats with deployable solar panels in different attitudes. The uncertainties for each estimated state component in tests using ROE1 are provided in Table 5. There are three main conclusions that can be drawn from this table. First, the semimajor axis can be estimated with an uncertainty of better than 100m in addition to the ROE for both relative orbits, indicating that knowledge of the effects of SRP improves observability for in-train formations. Second, it is clear that B_o cannot be estimated with useful accuracy. Third, including δB in the estimated state increases the range uncertainty by a factor of five for ROE1 much more in ROE2. It is clear from this behavior that accurate knowledge of the differential ballistic coefficient is required to accurately estimate the inter-spacecraft separation in GEO.

Noting the importance of the differential ballistic coefficient, covariance matrices were recomputed for with δB values ranging from 0.0001 to 0.02 to span the full range of possible values for applications of interest. The considered state subsets include 1) only the ROE, and 2) the ROE and the semimajor axis. Table 6 includes computed uncertainties for $\delta\lambda$ in each of these tests. It is clear from this table that a large value of δB improves observability in all test cases, particularly for ROE2 (in-train formation) when the semimajor axis is included in the state estimate.

The combined results in Tables 5 and 6 show that accurate estimation of the range to a resident space object in GEO with only a few orbits of measurements is achievable if the differential ballistic coefficient is nonzero and known with sufficient accuracy. This behavior is consistent with the improvements in range observability when maneuvers are performed.[13,19] Indeed, the range uncertainty when δB is near zero is five times larger than in LEO due to the increased orbit radius.

Table 5. Uncertainties for each subset of estimated states with two orbits of measurements in GEO for ROE1 configuration.

ROE	1	1	1	1	2	2	2	2
$a\sigma_{\delta a}$ (m)	0.5	0.9	0.9	2.6	0.5	1.0	1.0	113.9
$a\sigma_{\delta\lambda}$ (km)	0.8	0.8	0.8	4.1	0.8	0.8	0.8	192.4
$a\sigma_{\delta e_x}$ (m)	1.2	1.3	1.5	1.2	1.2	1.3	1.5	1.2
$a\sigma_{\delta e_y}$ (m)	29.3	30.3	30.7	162.5	29.3	1.0	1.1	1.6
$a\sigma_{\delta i_x}$ (m)	0.7	0.7	0.7	0.7	0.7	0.7	0.7	0.7
$a\sigma_{\delta i_y}$ (m)	30.0	31.1	31.3	162.3	30.0	0.7	0.7	0.7
σ_a (m)	-	75.1	-	-	-	81.7	-	-
σ_B (m^2/kg)	-	-	0.041	-	-	-	0.047	-
$\sigma_{\delta B}$ (m^2/kg)	-	-	-	0.001	-	-	-	0.0381

Table 6. Variation of $a_o\sigma_{\delta\lambda}$ (km) in GEO for selected values of δB.

		a not estimated		a estimated	
# orbits		ROE1	ROE2	ROE1	ROE2
	0.0001	3.8	3.8	4.3	81.4
	0.0002	3.7	3.7	4.2	40.7
	0.0005	3.5	3.5	3.9	16.3
δB	0.001	3.1	3.1	3.5	8.1
(m^2/kg)	0.002	2.4	2.4	2.7	4.1
	0.005	1.4	1.4	1.5	1.6
	0.01	0.8	0.8	0.8	0.8
	0.02	0.4	0.4	0.4	0.4

Summary

Overall, these results suggest that the semimajor axis of the observer's orbit is strongly observable in a wide range of orbit regimes. Under the assumptions of perfect dynamics knowledge and perfect knowledge of non-estimated state components, the semimajor axis can be estimated with uncertainty of less than 100m with minimal impact on relative navigation accuracy. Uncertainties in other orbit elements are on the order of hundreds of meters or more even under these optimistic assumptions, suggesting that realistic estimation errors will be impractically large. Accordingly, it is necessary to rely on a-priori information for these state components. It was also found that formation geometries with significant motion in the plane perpendicular to the flight direction are more observable with angles-only measurements than in-train formations.

IROD ALGORITHM DESCRIPTION

The algorithm proposed in this paper proceeds in two steps. First, an estimate of the ROE and semimajor axis is computed from an a-priori guess of the observer's absolute orbit (nominally provided by the ground using TLEs, the Deep Space Network, or some onboard sensor) and a batch of time-tagged bearing angle measurements to the target. Second, the covariance of the estimated state is computed using the converged measurement residuals and the covariance associated with the a-priori information. The procedures for each of these computations are described in the following.

State Estimation

The observability analysis in the previous section demonstrated that the observer's semimajor axis and all ROE except for $\delta\lambda$ are strongly observable and $\delta\lambda$ (which captures the range to the target) is weakly observable. Leveraging this result, the state estimate is computed using a practical approach inspired by the works of Gaias[24] and Ardaens[19] that estimates strongly observable elements using iterative batch least

squares and the weakly observable range through sampling. First, the user selects a set of samples of $\delta\lambda$ based on the mission scenario (i.e. expected minimum and maximum separations). For each $\delta\lambda$ sample, a complete state estimate is computed by using iterative batch least squares to estimate the strongly observable state components. For the first $\delta\lambda$ sample, the estimated state $\boldsymbol{x}_{est}$ is initialized as follows. The semimajor axis is set to the value from the a-priori guess of the observer's absolute orbit and all ROE except for $\delta\lambda$ are set to zero. For subsequent $\delta\lambda$ samples, the ROE are initialized as the previous converged solution scaled by the ratio of the current sample of $\delta\lambda$ to the previous sample. This saves computation effort as the direction of the converged ROE estimates does not change significantly between adjacent $\delta\lambda$ samples. Similarly, the semimajor axis is initialized to the previous converged value. More explicitly, the new initial values of the ROE ($\delta\boldsymbol{\alpha}^+$) and semimajor axis ($a^+$) are computed from the previous converged estimates $\delta\boldsymbol{\alpha}_f^-$ and a_f^- as given by

$$\delta\boldsymbol{\alpha}^+ = \delta\boldsymbol{\alpha}_f^- \frac{\delta\lambda^+}{\delta\lambda^-} \qquad a^+ = a_f^- \tag{15}$$

where $\delta\lambda^+$ denotes the new sample and $\delta\lambda^-$ denotes the previous sample.

The values of δa, δe_x, δe_y, δi_x, δi_y, and a are refined using the iterative batch least squares update formulated as

$$\begin{aligned} \Delta\boldsymbol{x}_{est} &= (\mathbf{Y}_{est}^T(\boldsymbol{x}_{k-1})\mathbf{Y}_{est}(\boldsymbol{x}_{k-1}))^{-1}\mathbf{Y}_{est}^T(\boldsymbol{x}_{k-1})(\boldsymbol{y}^{true} - \boldsymbol{g}(\boldsymbol{x}_{k-1}, t_{est}, \boldsymbol{t}_m)) \\ \boldsymbol{x}_k &= \boldsymbol{x}_{k-1} + \begin{pmatrix} \Delta\boldsymbol{x}_{est} \\ \mathbf{0} \end{pmatrix} \end{aligned} \tag{16}$$

where $\boldsymbol{y}^{true}$ is the provided batch of bearing angle measurements. These iterations proceed until either a user-specified number of iterations is exceeded or the state increment satisfies user-specified termination conditions (e.g. $\Delta\boldsymbol{x}_{est}$ is small enough that the resulting change in the modeled measurements is negligible). After the batch least squares refinement terminates, the norm of the measurement residual vector is computed and saved.

Once state estimates for all $\delta\lambda$ samples are computed, the final state estimate is selected as the candidate with the smallest measurement residual vector. As demonstrated by Ardaens,[19] the norm of the measurement residual is normally a convex function of the range, but the slope of this metric in the vicinity of the minimum is a function of measurement errors, dynamics model errors, formation geometry, whether maneuvers are performed, and other considerations.

Uncertainty Estimation

The uncertainty associated with the estimated state is estimated using a novel approach that minimizes reliance on a-priori sensor characterization and accounts for uncertainty in the a-priori information. To accomplish this, it is first necessary to compute an estimate of the noise matrix for the complete batch of measurements $\mathbf{R}_{est} \in \mathbb{R}^{2N\times 2N}$. This estimate is computed in two steps. First, the noise matrix for each individual measurement $\mathbf{R}_{post} \in \mathbb{R}^{2\times 2}$ (which is assumed constant) is computed from the post-fit measurement residuals as given by

$$\mathbf{R}_{post} = \frac{1}{N}\sum_{j=1}^{N}(\boldsymbol{z}^{true}(t_j) - \boldsymbol{h}(\boldsymbol{x_f}, t_{est}, t_j))(\boldsymbol{z}^{true}(t_j) - \boldsymbol{h}(\boldsymbol{x_f}, t_{est}, t_j))^T \tag{17}$$

where $\boldsymbol{x}_f$ denotes the converged state estimate. This approach enables the algorithm to operate without an accurate a-priori model of the sensor noise characteristics. Second, the noise matrix for the complete set of measurements is computed by adding the sensor noise matrix to the noise due to uncertainty in the a-priori information as given by

$$\mathbf{R}_{est} = N\begin{bmatrix} \mathbf{R}_{post} & \mathbf{0} & \dots & \mathbf{0} \\ \mathbf{0} & \mathbf{R}_{post} & \dots & \mathbf{0} \\ \vdots & \vdots & \ddots & \vdots \\ \mathbf{0} & \mathbf{0} & \dots & \mathbf{R}_{post} \end{bmatrix} + \mathbf{Y}_{prior}(\boldsymbol{x}_f)\mathbf{P}_{prior}\mathbf{Y}_{prior}^T(\boldsymbol{x}_f) \tag{18}$$

where $\mathbf{P}_{prior}$ and $\mathbf{Y}_{prior}$ do not include terms related to the semimajor axis because it is part of the estimated state. The sensor noise matrix is multiplied by a factor of N because it was found in simulations that estimation error is generally independent of the number of measurements as long as at least 10 measurements per orbit are available. Accordingly, this modification provides uncertainties that are more consistent with estimation errors in a wide range of scenarios. Finally, the covariance for the estimated state $\mathbf{P}_f$ (including all ROE and the semimajor axis) is computed from $\mathbf{Y}_{est}(\boldsymbol{x_f})$ and $\mathbf{R}_{est}$ as given by

$$\mathbf{P}_f = (\mathbf{Y}_{est}^T(\boldsymbol{x_f})\mathbf{Y}_{est}(\boldsymbol{x_f}))^{-1}(\mathbf{Y}_{est}^T(\boldsymbol{x_f})\mathbf{R}_{est}\mathbf{Y}_{est}(\boldsymbol{x_f}))(\mathbf{Y}_{est}^T(\boldsymbol{x_f})\mathbf{Y}_{est}(\boldsymbol{x_f}))^{-1} \tag{19}$$

This formulation allows the behavior of the uncertainty to seamlessly transition between regimes in which noise is dominated by uncertainty in the a-priori information (e.g. km-level errors from a NORAD TLE estimate) and when noise is dominated by the sensor.

VALIDATION

The proposed algorithm is validated through Monte Carlo simulations of scenarios in LEO, Mars orbit, and GEO. The initial absolute orbits of the observer in these orbit regimes are specified in Table 1. The test cases are selected to demonstrate that the algorithm provides accurate state estimates across a wide range of orbit regimes with different perturbations. To ensure a fair comparison across orbit regimes, the measurement rates for each simulation are selected to ensure that 50 bearing angles are provided per orbit. Accordingly, bearing angle measurements are provided every 120s in LEO, 480s in Mars orbit, and 1800s in GEO for two orbits. The perturbations and time steps for each orbit are the same as those used in the observability analysis.

The Monte Carlo simulations are intended to provide a statistical characterization of the estimation errors and their sensitivity to errors in the a-priori information. For each simulation, the algorithm inputs including a-priori state information (observer's orbit, absolute ballistic coefficient, and differential ballistic coefficient) and the batch of bearing angle measurements to the target are computed using the following procedure:

1. The a-priori observer's orbit and absolute and differential ballistic coefficients at the estimation epoch are computed by corrupting the user-specified ground truth values with zero-mean Gaussian noise with a user-specified distribution.
2. The osculating orbits of the observer and target are propagated to each measurement epoch using a high-fidelity numerical orbit propagator[22] including all significant perturbations in each orbit (key models and parameters are specified in Table 7).
3. Bearing angle measurements are computed for each measurement epoch by corrupting the true bearing angles for the user-specified sensor attitude with zero-mean Gaussian noise with 1-σ errors of 20arcsec.

The initial ground truth ROE for each test case are randomly sampled from a distribution with the following properties: 1) $a\delta\lambda$ is uniformly distributed between 50km and 150km, 2) the magnitudes of the relative eccentricity and inclination vectors are uniformly distributed between 1% and 2% of $\delta\lambda$ to ensure uniform observability between all test cases in all orbit regimes, 3) the phase angles of the relative eccentricity and inclination vectors are uniformly distributed between 0 and 2π, and 4) $a\delta a$ is uniformly distributed between -100m and 100m. This distribution is also representative of relative orbits that are expected in the StarFOX experiment.[14,21] Also, the ground truth ballistic coefficient of the observer is set at 0.005m^2/kg and the differential ballistic coefficient is sampled from a uniform distribution between 0.01 and 0.02m^2/kg to provide adequate observability at large separations in GEO.

The algorithm parameters used throughout these simulations are as follows. The estimation epoch is set to the initial epoch for the simulation (see Table 7). The sampling of $a\delta\lambda$ is from 2km to 200km in 2km intervals. The maximum number of refinement iterations for each candidate solution is five. The iteration procedure terminates if the following two conditions are satisfied: 1) the largest change in any single ROE is less than 0.1m/a, and 2) the change in the semimajor axis is less than 1m.

The performance of each test case is assessed by four error metrics. The first metric of interest is the range error ϵ_{range}, which is the weakly observable part of the relative state. The second error metric is the

Table 7. Numerical orbit propagator models and parameters.

Common Parameters	
Integrator	Runge-Kutta Dormand-Prince
Step size	30s
Initial Epoch	January 1, 2017 00:00:00
Earth Orbit	
Geopotential	GRACE Gravity Model 01S 60×60[1]
Atmospheric density	Harris-Priester[29]
Solar radiation pressure	Flat plate with conical Earth shadow
Third-body gravity	Lunar and solar point masses, analytic ephemerides
Mars Orbit	
Geopotential	Gravity Model GMM3 60×60[28]
Solar radiation pressure	Flat plate with conical Mars shadow
Third-body gravity	Solar point mass with analytic ephemerides

pointing vector error ϵ_{unit}, which is a metric of the maximum error in the other ROE that is not due to range error. This error is expressed in units of meters of error per meter of separation (e.g. 0.001m/m corresponds to 0.001m of error per 1m separation). The third error metric is the error in the semimajor axis ϵ_a. The final metric is the Mahalanobis distance ϵ_{mahal}, which is a metric of the consistency of the estimation error and the computed uncertainty. The distribution of ϵ_{mahal} for each set of simulations should be similar to the Mahalanobis distance distribution for Gaussian random variable of dimension seven (since the estimated state includes 6 ROE and the semimajor axis). These error metrics are formally defined as

$$\begin{aligned} \epsilon_{range} &= a_o \Big| ||\delta\boldsymbol{\alpha}_f|| - ||\delta\boldsymbol{\alpha}_{true}|| \Big| \qquad \epsilon_{unit} = \Big|\Big| \frac{\delta\boldsymbol{\alpha}_f}{||\delta\boldsymbol{\alpha}_f||} - \frac{\delta\boldsymbol{\alpha}_{true}}{||\delta\boldsymbol{\alpha}_{true}||} \Big|\Big| \\ \epsilon_a &= |a_f - a_{true}| \qquad \epsilon_{mahal} = \sqrt{(\boldsymbol{x}_{true} - \boldsymbol{x}_f)^T \mathbf{P}_f^{-1} (\boldsymbol{x}_{true} - \boldsymbol{x}_f)} \end{aligned} \tag{20}$$

where ground truth quantities are denoted by the subscript $true$ and final estimates produced by the algorithm are denoted by the subscript f.

LEO Results

The robustness of the proposed algorithm to errors in the a-priori information is assessed by running 100 simulations for each of five error distributions for the a-priori absolute orbit information. The covariance matrix $\mathbf{P}_{\boldsymbol{\alpha}}$ for each of these distributions is of the form

$$\mathbf{P}_{\boldsymbol{\alpha}} = \epsilon^2 \begin{pmatrix} 1 & 0 & 0 & 0 & 0 & 0 \\ 0 & a^{-2} & 0 & 0 & 0 & 0 \\ 0 & 0 & a^{-2} & 0 & 0 & 0 \\ 0 & 0 & 0 & a^{-2} & 0 & 0 \\ 0 & 0 & 0 & 0 & a^{-2} & 0 \\ 0 & 0 & 0 & 0 & 0 & a^{-2} \end{pmatrix} \tag{21}$$

where ϵ takes one of the following values: 200m, 500m, 1000m, 2000m, 5000m. Each simulation took between 195 and 269 seconds to run in MATLAB on a desktop PC with a 3.5GHz clock speed, which is more than ten times faster than the $>$1hr times reported by Ardaens using a numerical dynamics model.[8] The total number of batch least squares refinement steps (i.e. uses of Equation (16)) ranged between 202 and 279 across all simulations, for an average of 2.4 steps per $\delta\lambda$ sample. The cumulative distribution functions (CDFs) for the four error metrics from simulations with each of these noise distributions are provided in Figure 2.

The first conclusion that can be drawn from this plot is that the distributions of ϵ_{mahal} closely follow the reference Gaussian distribution for all error levels, indicating that the computed uncertainties and estimation

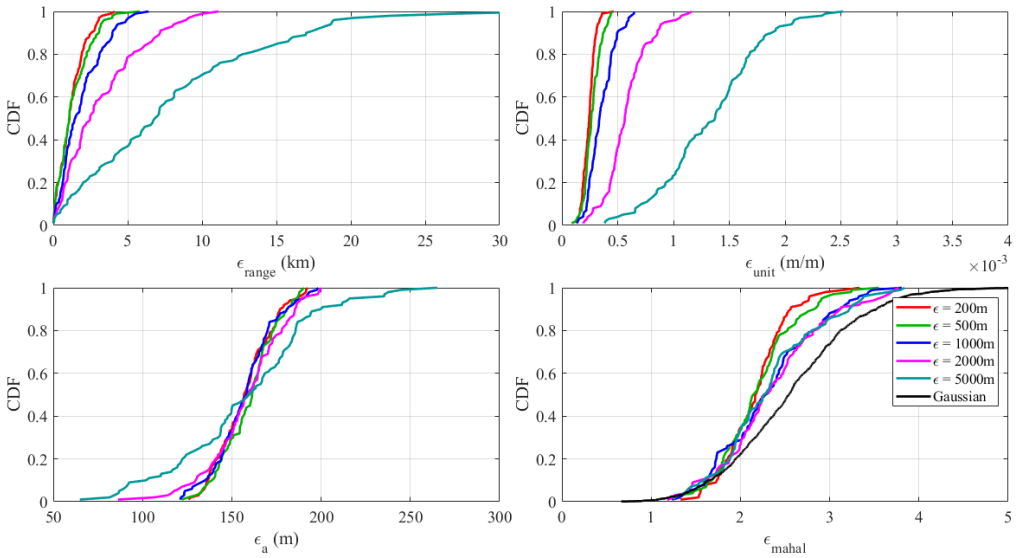

Figure 2. CDFs for error metrics from simulations in LEO with selected noise levels applied to a-priori absolute orbit information. A reference 7D Gaussian distribution is shown in black for comparison with Mahalanobis distance distributions.

errors are statistically consistent. Next, it is evident that the 3-sigma range error is less than 20% of the means separation of 100km for all simulations where $\epsilon \leq 2$km. Also, the 1-sigma range error is at least 2ϵ for all simulations, suggesting that the range estimation error is limited by errors in the knowledge of the mean argument of latitude of the observer due to the aforementioned poorly observable mode. The distributions of ϵ_{unit} indicates that the estimation accuracy for the other ROE is no worse than 2.5m per kilometer of separation in all simulations. Finally, the error in the semimajor axis is no larger than 270m in all simulations. It should be noted that there is a persistent bias of 125m in the semimajor axis estimates, which is believed to be due to numerical integration error. It should be possible to reduce this error with a smaller timestep or better numerical integration scheme. Overall, these results show that the proposed algorithm can provide accurate estimates of the relative orbit of the target and the observer's semimajor axis in the presence of kilometer-level errors in a-priori orbit knowledge. The authors have also implemented the algorithm with an analytical dynamics model for J_2-perturbed orbits and achieved similar estimation accuracy with a run time of only five seconds. Accordingly, it is recommended to use analytical dynamics models in any orbit regime for which a sufficiently accurate model is available.

Mars Orbit Results

Sets of 100 Monte Carlo simulations were conducted for Mars orbit using the same error distributions for the a-priori orbit knowledge used in LEO simulations. The run times for the algorithm varied from 522 to 630 seconds. This increase over the computation time in LEO simulations is expected these simulations require twice as many integration steps of the dynamics model. The CDFs for the error metrics for all mars orbit simulations are provided in Figure 3.

As in the LEO simulations, the Mahalanobis distance distributions closely agree with the reference Gaussian distribution, meaning that the estimation uncertainties and errors are statistically consistent. The distributions of range errors are nearly identical to those in LEO orbits. The semimajor axis errors are roughly double the errors in LEO and show a persistent bias of approximately 250m that does not vary with a-priori orbit error. This behavior suggests that the bias is due to numerical integration error and can be improved by using smaller time steps or a better numerical integration scheme. Finally, the distributions of ϵ_{unit} indicates that the estimation accuracy for the other ROE is better than 2m per kilometer of separation in all

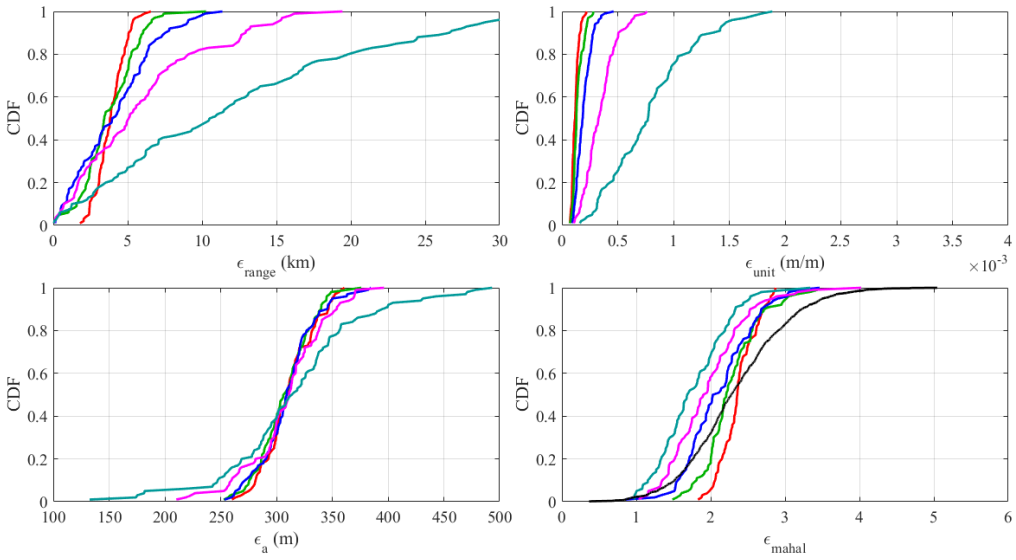

Figure 3. CDFs for error metrics from simulations in Mars orbit with selected noise levels applied to a-priori absolute orbit information. A reference 7D Gaussian distribution is shown in black for comparison with Mahalanobis distance distributions.

simulations. Overall, these results show that the algorithm provides accurate state estimates and statistically consistent uncertainties in eccentric orbits and orbits around other planetary bodies.

GEO Results

As in LEO and mars orbit, sets of 100 simulations are conducted in GEO for various levels of error in the a-priori information including the absolute orbit as well as the absolute and differential ballistic coefficients. For simplicity, it is assumed that ϵ is 1000m for all simulations as it has already been established that this error does not significantly degrade estimation accuracy. The a-priori value of B_o is subject to 1-σ errors of 10% of the ground truth value, which can be achieved with on-orbit calibration using an external reference metrology. Finally, the a-priori value of δB is subject to 1-σ errors of 2%, 5%, and 10% of its ground truth value. While providing such accurate estimates of δB would be challenging for some applications (e.g. rendezvous with a poorly characterized target), the results of the observability analysis suggest that minimizing this error is critical for accurate range estimation over short timescales. The run times for the algorithm ranged from 107 to 138 seconds for these simulations. As the total number of batch least squares refinement steps ranged between 227 and 265, it is evident that the computation time is proportional to the total number of evaluations of the perturbing accelerations in the dynamics model. The CDFs for the error metrics for all GEO simulations are provided in Figure 4.

Unlike the LEO and Mars orbit tests, the distributions of ϵ_{mahal} are closer to a 1D Gaussian distribution, suggesting that a less conservative estimate can be used for these scenarios. Also, it is clear that the range error increases roughly linearly with the error in δB as expected from the observability analysis. The semimajor axis is always estimated with an accuracy of better than 400m and shows no sensitivity to error in δB. Finally, ϵ_{unit} is always less than 5×10^{-4}m/m, indicating that all terms other than the range are very well-known. Overall, these results show that the proposed algorithm can provide accurate estimates of the relative orbit of a target resident space object in orbits perturbed by non-conservative forces as long as the differential ballistic coefficient is known with sufficient accuracy.

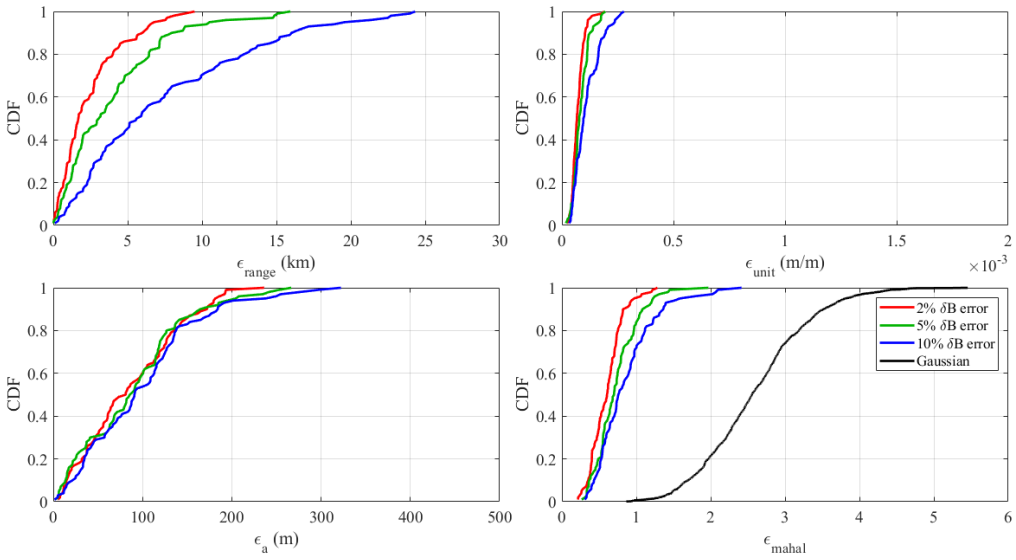

Figure 4. CDFs for error metrics from simulations in GEO with selected noise levels applied to the a-priori differential ballistic coefficient. A reference 7D Gaussian distribution is shown in black for comparison with Mahalanobis distance distributions.

Summary

The conducted simulations demonstrated that the proposed algorithm is able to accurately estimate the relative orbit of a resident space object in a wide range of orbit regimes with different perturbations. Unlike previous approaches, the algorithm is able to provide accurate relative state estimates in the presence of kilometer-level errors in the a-priori knowledge of the observer's absolute orbit and the absolute and differential ballistic coefficients. The algorithm requires a few minutes of computation time on a desktop PC, but expected that this can be reduced by 1) a better numerical integration scheme, 2) a more sophisticated sampling algorithm that reduces the total number of computed state estimates, and 3) use of analytical dynamics models when available. With these improvements, it is expected that this algorithm will enable for the first time autonomous onboard initialization of an angles-only navigation filter in the StarFOX experiment on the Starling1 mission.[14,21]

CONCLUSIONS

This paper proposes a novel numerical solution to the problem of estimating the relative orbit of a resident space object and its uncertainty using angles-only measurements from a single monocular camera. To meet this objective, a quantitative observability analysis is conducted to determine what components of the absolute orbit can be estimated in addition to the relative orbit using angles-only measurements. This analysis resulted in three key findings. First, the semimajor axis of the absolute orbit is strongly observable in all considered orbits and can be estimated with an accuracy of a few hundred meters or better. Second, there is a particularly weakly observable mode that includes the range and the mean argument of latitude. As such, the achievable accuracy of the range estimate will be limited by the error in the a-priori knowledge of the mean argument of latitude. Third, the range is nearly indistinguishable from the relative semimajor axis for in-train formations in near-circular orbits. Accordingly, mitigations such as maneuvers or use of multiple observers will be required for these configurations. However, in-train formation geometry does not compromise observability in eccentric orbits.

Next, an algorithm was proposed to estimate the relative orbit of a resident space object, the semimajor axis of the observer's orbit, and corresponding uncertainties. The algorithm estimates the weakly observable

range through a sampling approach and the remaining strongly observable state components using iterative batch least squares refinement. The algorithm was validated through high-fidelity Monte Carlo simulations of scenarios representative of formation flying missions in low earth orbit, geostationary orbit, and mars orbit. These simulations demonstrated that the algorithm is able to provide range estimates with errors of no larger than 20% with up to 2km 1-σ errors in the a-priori orbit information. Additionally, the other relative orbital elements are always estimated with an accuracy of better than three meters of error per kilometer of separation. Finally, the estimation errors are shown to be statistically consistent with the computed uncertainties.

Overall, these simulation results show that the proposed algorithm is able to accurately estimate the relative orbit of a target using bearing angle measurements from a single camera and a coarse estimate of the observer's orbit and ballistic properties in a wide range of orbit regimes and perturbation environments. The algorithm can be used in any planetary orbit regime as long as accurate models of the dominant perturbations are available. With these capabilities, the proposed algorithm can enable fully autonomous angles-only navigation in the StarFOX experiment and future missions orbiting other planetary bodies.

ACKNOWLEDGMENTS

This work was supported by the NASA Small Spacecraft Technology Program (cooperative agreement number 80NSSC18M0058) for contribution to the Starling-1/StarFOX efforts.

REFERENCES

[1] B. D. Tapley, S. Bettadpur, M. Watkins, and C. Reigber, "The Gravity Recovery and Climate Experiment: Mission Overview and Early Results," *Geophysical Research Letters*, Vol. 31, No. 9, 2004.

[2] G. Krieger, A. Moreira, H. Fiedler, I. Hajnsek, M. Werner, M. Younis, and M. Zink, "TanDEM-X: A Satellite Formation for High-Resolution SAR Interferometry," *IEEE Transactions on Geoscience and Remote Sensing*, Vol. 45, No. 11, 2007, pp. 3317–3341.

[3] S. D'Amico, J.-S. Ardaens, and R. Larsson, "Spaceborne Autonomous Formation-Flying Experiment on the PRISMA Mission," *Journal of Guidance, Control, and Dynamics*, Vol. 35, May 2012, pp. 834–850, 10.2514/1.55638.

[4] J. Burch, T. Moore, R. Torbert, and B. Giles, "Magnetospheric Multiscale Overview and Science Objectives," *Space Science Reviews*, Vol. 199, No. 1-4, 2016, pp. 5–21.

[5] S. D'Amico, J.-S. Ardaens, G. Gaias, H. Benninghoff, B. Schlepp, and J. L. Jørgensen, "Noncooperative Rendezvous Using Angles-Only Optical Navigation: System Design and Flight Results," *Journal of Guidance, Control, and Dynamics*, Vol. 36, Nov. 2013, pp. 1576–1595, 10.2514/1.59236.

[6] G. Gaias, J.-S. Ardaens, and S. D'Amico, "The Autonomous Vision Approach Navigation and Target Identification (AVANTI) Experiment: Objectives and Design," *9th International ESA Conference on Guidance, Navigation & Control Systems, Porto, Portugal*, 2014.

[7] G. Gaias and J.-S. Ardaens, "Flight Demonstration of Autonomous Noncooperative Rendezvous in Low Earth Orbit," *Journal of Guidance, Control, and Dynamics*, Vol. 41, No. 6, 2017, pp. 1337–1354.

[8] J.-S. Ardaens and G. Gaias, "Angles-Only Relative Orbit determination in Low Earth Orbit," *Advances in Space Research*, Vol. 61, No. 11, 2018, pp. 2740–2760.

[9] D. C. Woffinden and D. K. Geller, "Observability Criteria for Angles-Only Navigation," *IEEE Transactions on Aerospace and Electronic Systems*, Vol. 45, No. 3, 2009, pp. 1194–1208.

[10] D. K. Geller and I. Klein, "Angles-Only Navigation State Observability during Orbital Proximity Operations," *Journal of Guidance, Control, and Dynamics*, Vol. 37, No. 6, 2014, pp. 1976–1983.

[11] T. A. Lovell and T. Lee, "Nonlinear Observability for Relative Satellite Orbits with Angles-Only Measurements," *24 th International Symposium on Space Flight Dynamics*, 2014.

[12] Y. Hu, I. Sharf, and L. Chen, "Three-Spacecraft Autonomous Orbit Determination and Observability Analysis with Inertial Angles-Only Measurements," *Acta Astronautica*, Vol. 170, 2020, pp. 106–121.

[13] J. Sullivan, T. A. Lovell, and S. D'Amico, "Angles-Only Navigation for Autonomous On-Orbit Space Situational Awareness Applications," *AAS/AIAA Astrodynamics Specialist Conference, Snowbird, UT*, 2018.

[14] J. Sullivan, A. W. Koenig, J. Kruger, and S. D'Amico, "Generalized Angles-Only Navigation Architecture for Autonomous Distributed Space Systems," *Journal of Guidance, Control, and Dynamics*, 2020. Submitted.

[15] A. W. Koenig, T. Guffanti, and S. D'Amico, "New State Transition Matrices for Relative Motion of Spacecraft Formations in Perturbed Orbits," *Journal of Guidance, Control, and Dynamics*, Sept. 2016, 10.2514/6.2016-5635.

[16] T. Guffanti, S. D'Amico, and M. Lavagna, "Long-Term Analytical Propagation of Satellite Relative Motion in Perturbed Orbits," *27th AAS/AIAA Space Flight Mechanics Meeting*, San Antonio, TX, 2017.

[17] Garg and Sinclair, "Initial Relative Orbit Determination Using Second-Order Dynamics and Line-of-Sight Measurements," 2015.

[18] D. K. Geller and T. A. Lovell, "Angles-Only Initial Relative Orbit Determination Performance Analysis using Cylindrical Coordinates," *The Journal of the Astronautical Sciences*, Vol. 64, No. 1, 2017, pp. 72–96.

[19] J.-S. Ardaens and G. Gaias, "A numerical approach to the problem of angles-only initial relative orbit determination in low earth orbit," *Advances in Space Research*, Vol. 63, No. 12, 2019, pp. 3884–3899.

[20] J. Kruger and S. D'Amico, "Autonomous Angles-Only Multi-Target Tracking for Spacecraft Swarms," *IEEE Transactions on Aerospace and Electronic Systems*, 2020. Submitted.

[21] H. Sanchez, D. McIntosh, H. Cannon, C. Pires, M. Field, J. Sullivan, S. D'Amico, L. Mall, and B. O'Connor, "Starling-1: Swarm Technology Demonstration," *32nd Annual Small Satellite Conference*, Logan, UT, Aug. 2018.

[22] V. Giralo and S. D'Amico, "Development of the Stanford GNSS Navigation Testbed for Distributed Space Systems," *Institute of Navigation, International Technical Meeting*, 2018.

[23] S. D'Amico, *Autonomous Formation Flying in Low Earth Orbit.* PhD Thesis, Delft University, 2010. OCLC: 839641932.

[24] G. Gaias, S. D'Amico, and J.-S. Ardaens, "Angles-Only Navigation to a Noncooperative Satellite Using Relative Orbital Elements," *Journal of Guidance, Control, and Dynamics*, Vol. 37, Mar. 2014, pp. 439–451, 10.2514/1.61494.

[25] A. Chicarro, P. Martin, and R. Trautner, "The Mars Express mission: an overview," *Mars Express: The Scientific Payload*, Vol. 1240, 2004, pp. 3–13.

[26] S. D'Amico and O. Montenbruck, "Proximity Operations of Formation-Flying Spacecraft Using an Eccentricity/Inclination Vector Separation," *Journal of Guidance, Control, and Dynamics*, Vol. 29, May 2006, pp. 554–563, 10.2514/1.15114.

[27] S. Palo, G. Stafford, and A. Hoskins, "An Agile Multi-Use Nano Star Camera for Constellation Applications," *Proceedings of the Small Satellite Conference, Advanced Technologies II, SSC13-III-5*, 2013.

[28] A. Genova, S. Goossens, F. G. Lemoine, E. Mazarico, G. A. Neumann, D. E. Smith, and M. T. Zuber, "Seasonal and static gravity field of Mars from MGS, Mars Odyssey and MRO radio science," *Icarus*, Vol. 272, 2016, pp. 228–245.

[29] O. Montenbruck and E. Gill, *Satellite Orbits: Models, Methods and Applications*. Springer, 2012.